Journal of the Chinese Society of Mechanical Engineers, Vol.47, No.1, pp49~58 (2026)

Study on the Meshing Impacts of Gear and Rack Systems of Pumping Machines by SPH-FEM Coupling Method

Xing-Jia Tang*, Mutellip Ahmat**and Fan-Kai Di*

Keywords: Gear and rack systems, SPH-FEM coupling method, Meshing impact, Microscopic wear mechanism, Miniaturized modeling experiment

ABSTRACT

This paper aims to explore the adaptability of the SPH-FEM coupling method in simulating gear and rack meshing impacts. Taking the gears and racks of a pumping unit as the research object, the adaptive SPH-FEM coupling method is used to simulate gear and rack meshing impacts. This provides a new approach for studying the impact of gear mechanisms that may involve structural damage. The propagation law of the impact stress is obtained, which reveals the microscopic mechanism of formation of the tooth-face impact wear and deduces that the metal debris generated in the meshing impact process is the main reason for the appearance of tooth surface defects. The results show that the peak residual stresses in section I and section II are 6.694×10^2 MPa and 2.935×10^2 MPa, respectively, after impacting for 0.6 ms, and the error of micro-experiment verification is very small, which indicates that the method is effective.

INTRODUCTION

With the increase in the difficulty of oil extraction, it is gradually difficult for traditional traveling beam pumping machines to meet the needs of oil fields (Peng et al., 2012). The gear and rack pumping machine has been widely used in oilfields in various regions due to the advantages of a large stroke, deeper extractable depth, higher extraction efficiency, and easier maintenance. However, due to the harsh field operating environment, gear and rack open operation, long-term heavy load, and other factors, the gear and rack mechanism is prone to severe meshing impacts, resulting in increased vibration of the whole mechanism, severe wear of the tooth surface, and even serious accidents such as broken gear teeth (Jia et al., 2020). These problems have aroused great concern in business and academic circles, and numerous studies have been carried out.

For the meshing impact of gears, many scholars have done much research. For example, Zhou et al. (2008) derived the analytical equations of geometrical position and meshing impact force through the analysis of the gear transmission line external meshing mechanism and then established the meshing impact friction model. Wang et al. (2023) calculated the mesh-in impact excitation method of a loaded gear pair based on cylindrical collision theory and contact dynamics theory, and accurately calculated the mesh-in impact time and tooth pair mesh-in impact force. Hu et al. (2021) established the mesh-in impact model of the internal mesh gear pair and planetary gear train and accurately obtained the mesh-in impact point, the mesh-in impact time, and the mesh-in impact force through the method of load-toothed contact analysis (LTCA). An in-depth study of the meshing impact of planetary gear trains was carried out. Liu et al. (2022) proposed a three-dimensional loaded tooth contact analysis (3-DLTCA) model for double helical gears considering long-period asymmetric errors, based on which the meshing impact force of the current meshing tooth pair in each meshing cycle was calculated. In general, most of the studies are based on theoretical methods and finite element simulations (Han et al., 2022). As a matter of fact, the theoretical method is too complicated and the solution accuracy is slightly insufficient after multiple simplification treatments. FEM thanks to the development of computer technology, can achieve satisfactory results when facing most of the problems, both in terms of solution accuracy and solution efficiency. However, the gear and rack mechanism in this paper is loaded with heavy loads, so it may produce large deformation when meshing impact occurs, and even local material failure. The FEM is incompetent in dealing with large deformation problems, and the computational

Paper Received November, 2024. Revised March, 2025. Accepted April, 2025. Author for Correspondence: Mutellip Ahmat.

* *Graduate Student, School of Electrical Engineering, Xinjiang University, Urumqi 830063, China.*

** *Professor, School of Electrical Engineering, Xinjiang University, Urumqi 830063, China.*

accuracy is greatly reduced, or even cannot be solved (Tang et al., 2021).

Smooth particle hydrodynamics is a meshless method that has emerged in recent years with excellent large deformation handling capability and has been widely used. Rahimi et al. (2022) proposed a new computational method based on SPH for some challenging impact scenarios involving fast dynamics or large deformations. Wałęsa et al. (2022) completed a numerical simulation of the extrusion process of dry ice molds by SPH and verified the accuracy of the simulation results experimentally. Feng et al. (2022) proposed a new fully-coupled smooth particle hydrodynamics (SPH) formulation, which can efficiently simulate the effect of rainwater infiltration on the stability of unsaturated soil slopes, improve the computational efficiency and facilitate the implementation of infiltration boundary conditions. However, the SPH method is computationally inefficient and it is difficult to impose boundary conditions, making it difficult to analyze practical engineering problems like those in this paper. Considering that the FEM can exactly compensate for the defects of the SPH method, the two methods can be coupled to form the SPH-FEM coupling method, which works together on the meshing impact of the gear and rack. In fact, this method has been used to study practical engineering problems, and the method is classified into three types: adaptive, consolidation and contact (Qiang, 2017). Zhou et al. (2019) used the SPH-FEM contact coupling method to numerically investigate the bird strike damage of composite laminates and obtained more reliable results. Xiao et al. (2017) used the adaptive SPH-FEM coupling method to simulate the single disk cutter rock-breaking process, clarifying the expansion law of rock cracks and the splash path of rock chips. Ren et al. (2022) established the SPH-FEM contact coupling model of pile-soil, analyzed the force characteristics of spliced piles, realized the transition from pile installation to lateral loading, and predicted the ultimate horizontal bearing capacity. Zhang et al. (2012) used an improved adaptive SPH-FEM coupling algorithm to carry out full-size three-dimensional numerical calculations of 7.62 mm rifle bullet impact on a special heat-treated 30CrMnSiA steel plate, which provides an effective way for calculating the impact of the low-strength bullet on the high-strength target plate.

In summary, the application of the SPH-FEM coupling method in the field of mechanical transmission such as gear and rack is still in its infancy, and the study of the meshing impact problem of gear and rack in this paper is imminent. At the same time, the adaptive SPH-FEM coupling method has higher computational accuracy and computational efficiency, and it is easy to implement the large-scale computational model. Therefore, the gear-and-rack pumping machine is taken as the engineering background, and the research is carried out with the gear-and-rack meshing impact as the research object and the adaptive SPH-FEM coupling method as the method.

ADAPTIVE SPH-FEM COUPLED MODELING

The principle of the adaptive SPH-FEM coupling algorithm is shown in Fig. 1. In Fig. 1, the solid line box is the finite cells that have not undergone large deformation, the dashed line box is the finite cells that have undergone large deformation, and the solid circle is the SPH particle. At the beginning of the computation, all objects in the computational domain are discretized into finite cells. As the computation time passes, when the finite cells undergo large deformation, they are converted to SPH particles to continue to complete the computation.

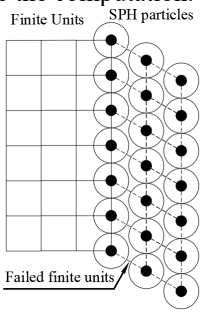

Fig. 1. Principle of the adaptive SPH-FEM coupling algorithm.

The newly generated SPH particles inherit the physical information of the corresponding finite cell nodes and execute the SPH integration format until the computation is completed (Qiang, 2017). The inheritance criterion is as follows:

$$\begin{cases} x_{\mathrm{p}} = x_{\mathrm{n}} \\ m_{\mathrm{p}} = m_{\mathrm{n}} = \sum_{i=1}^{N_{\mathrm{e}}} \dfrac{1}{N_{\mathrm{n}}} \rho_{\mathrm{e}i} V_{\mathrm{e}i} \\ v_{\mathrm{p}} = v_{\mathrm{n}} \\ \sigma_{\mathrm{p}} = \sigma_{\mathrm{n}} = \dfrac{1}{N_{\mathrm{e}}} \sum_{i=1}^{N_{\mathrm{e}}} \sigma_{\mathrm{e}i} = \dfrac{1}{N_{\mathrm{e}}} \sum_{i=1}^{N_{\mathrm{e}}} \sum_{j=1}^{N_{\mathrm{g}}} \omega_{\mathrm{g}j} \sigma_{\mathrm{g}j} \\ c_{\mathrm{p}} = c_{\mathrm{n}} \end{cases} \tag{1}$$

where x, m, ρ, V, v, σ, c are position, mass, density, volume, velocity, stress tensor and speed of sound; subscript p denotes an SPH particle, subscript n denotes a finite element node, subscript e denotes a finite cell, and subscript g denotes an integration point inside a finite cell; Ne is the number of finite cells associated with the node; Nn is the number of nodes of a single finite cell; Ng is the number of integration points inside a single finite cell.

The implementation of the SPH algorithm relies on the smooth length to determine the support domain of the particles, but the concept of smooth length does not exist in the finite element method, so it needs to

rely on the law of conservation of mass for calculation:

$$h_p = \frac{a}{N_e}\sum_{i=1}^{N_e} r_{0i}\left(\frac{\rho_{0i}}{\rho_i}\right)^{\frac{1}{d}} \quad (2)$$

where a is the ratio coefficient of smooth length to cell size; r_0 is the initial cell size; ρ_0 and ρ denote the initial and current densities, respectively; and d denotes the number of dimensions.

Computational Models

Taking an oilfield rack and pinion pumping machine in Xinjiang as an object, its working principle is shown in Fig. 2: the motor drives the gear to mesh with the annular rack and pinion, driving the pumping rod to reciprocate to extract crude oil. In the project, the rack running section is divided into straight line section, arc section and transition section I (straight line → arc), II (arc → straight line). Among them, the transition section is the focus of this study because of the easy occurrence of meshing impact.

After communicating with the maintenance engineer of the pumping unit, the geometric parameters of the gear and rack are obtained as shown in Table 1. The gear and rack are processed by wire cutting, and the gear material is 42CrMo steel (GB 42CrMo, ASTM 4142, DIN 42CrMo4); the rack material is 40Cr steel (GB 40Cr, ASTM 5140, DIN 41Cr4). After tempering, high-frequency quenching is carried out, so that the tooth surface hardness of the gear reaches HRC55-60, and the tooth surface hardness of the rack reaches HRC50-55. To improve the efficiency of the calculation, the redundant parts are omitted from the modeling, and only the gear and rack are retained. When the gear and rack have meshed into the impact, the tooth pair will be subjected to a large force, and the contact surface is very likely to be spalled or slipped. Therefore, it is necessary to densify the mesh in the contact area of the tooth pair, as shown in Fig. 3.

In view of the calculation accuracy and the SPH discretization requirements of the model, the finite element discretization of the gear and rack adopts first-order hexahedral elements. In the meshing analysis of the gear and rack, to ensure no interference between the gear and rack, frictional contact is set, with a friction coefficient of 0.1. The rack is fixed, and a torque of 3360 N·m is applied to the center of the gear through ramp loading to improve convergence.

The gear is in uniformly accelerated motion, and the torque is applied in a ramp-loading manner, increasing from 0 N·m to 3360 N·m.

To verify the accuracy of the calculation model, a static strength check is required. The model is imported into the static analysis software, the rack is fixed according to the pumping machine operation, the rotating vice is added to the gear center, the torque of 3360N·m is applied, and the contact is added between the pairs of teeth that may be in contact. The results of static strength calculation are shown in Figure 4.

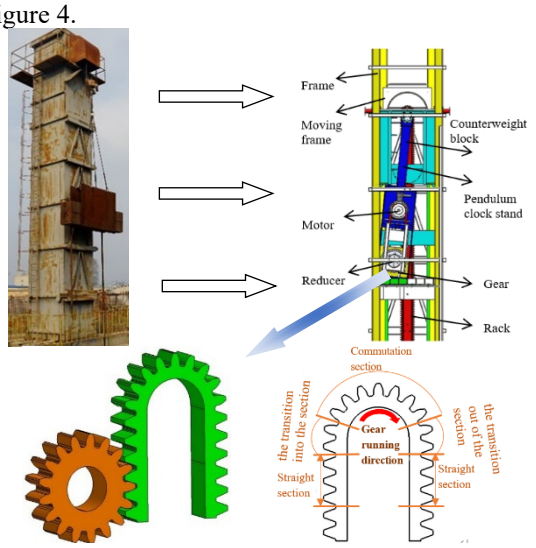

Fig. 2. Gear and rack structure of a pumping unit.

Table 1. Geometrical parameters of gear and rack.

Parts	Gear	Rack
Modulus m/mm	16	16
Number of teeth Z	17	290
Tooth width b/mm	110	110
Pressure angle α/deg	20	20
Spiral angle β/deg	0	0
Tooth top height factor	1	1
Top gap coefficient	0.25	0.25
Accuracy grade	7	8
Change in length of the common law line F_w/mm	0.036	0.125
Tooth shape tolerance f_f/mm	0.022	0.09
Tooth orientation tolerance F_β/mm	0.016	0.02
Limit deviation of tooth pitch f_{pt}/mm	0.025	0.05

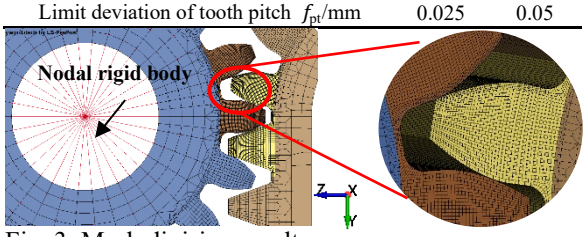

Fig. 3. Mesh division results.

Fig. 4 shows that the maximum tooth contact stress of the gear and rack is 145.10 MPa and the maximum tooth root bending stress is 49.065 MPa. Table 2 lists the calculation results under three different methods. Where, e_1 is the error between this paper and the theoretical calculation results, and e_2 is the error between this paper and the calculation results of the literature (Bai et al., 2022). The theoretical calculations were performed using the Hertzian contact theory and the bending stress formulae provided in the literature (Bai et al., 2022). It can be seen that e_1 and e_2 are less than 5%, indicating that the model is reliable in its calculation accuracy. On the other hand, it can be seen from the figure that the maximum tooth contact stress occurs near the gear indexing circle, which is consistent with the actual operation of the gear, indicating that the model has high assembly accuracy.

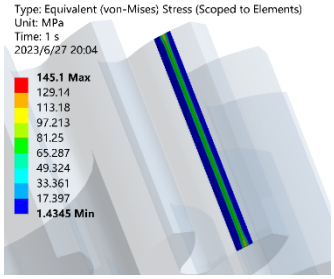

(a)

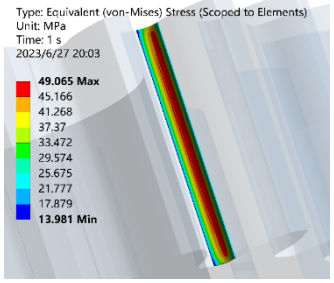

(b)

Fig. 4. Static strength checking results: (a) tooth contact stress cloud, (b) tooth root bending stress cloud.

Table 2. Static strength calibration results.

Calculation results	Contact stress σ_H/MPa	Bending stress σ_F/MPa
Simulation values	145.10	49.065
Theoretical values	143.72	48.708
Documentary values	147.89	48.54
e_1/%	0.96	0.73
e_2/%	1.99	1.08

Constitutive Model

The constitutive relationship is the most important factor affecting the accuracy of the numerical simulation solution (Kim et al., 2003). Both 42CrMo steel and 40Cr steel are typical elastic-plastic ontologies. The strain-hardening effect occurs when elastoplastic materials are subjected to large impact loads (Xin, 2020; Lu et al., 2016; Mustafa et al., 2007). The relationship between the strain rate and the dynamic yield stress of 42CrMo and 40Cr steels can be described by combining with the Cowper-Symonds model.

$$\sigma_Y = \left(\sigma_0 + \beta E_p \varepsilon_p^{eff}\right)\left[1+\left(\frac{\dot{\varepsilon}}{C}\right)^{\frac{1}{P}}\right] \quad (1)$$

where σ_0 is the initial yield stress, β is the hardening parameter, ε_p^{eff} is the effective plastic strain, C and P are the strain rate parameters, $\dot{\varepsilon}$ is the strain rate, and Ep is the plastic hardening modulus, which is given by

$$E_p = \frac{EE_t}{E-E_t} \quad (2)$$

Where E is the modulus of elasticity and E_t is the tangent modulus. Generally speaking, the tangent modulus of a material is not a fixed value and needs to be updated in real-time during the calculation process. However, the hardening curves of 42CrMo and 40Cr steels are relatively smooth, so the tangent modulus can be approximated according to the following equation

$$E_t = \frac{\sigma_b - \sigma_s}{\eta - \frac{\sigma_s}{E}} \quad (3)$$

where σ_s and σ_b are the yield strength and tensile strength of the material, respectively, and η is the elongation of the material. After consulting references (Xin, 2020; Guo, 2015), the parameters of the two materials are shown in Table 3.

Table 3. Material parameters of gear and rack.

Materials (GB)	42CrMo	40Cr
Densities ρ/kg·m^3	7850	7850
Young's modulus E/MPa	2.10×105	2.10×105
Poisson's ratio	0.3	0.3
Yield strength σ_s/MPa	930	880
Tensile strength σ_b/MPa	1040	1000
Elongation η/%	12	9
C/s^{-1}	40.4	42.7
P	5	4.7
β	1	1

NUMERICAL SIMULATION BASED ON THE ADAPTIVE SPH-FEM COUPLING METHOD

The numerical simulation is controlled by the rotational speed and load force. The rotational speed and load forces are applied to a nodal rigid body, which is generated by a part of the nodes on the gear hub at the geometric center of the gear, as shown in Fig. 3. It is known from the field investigation that the pumping unit of this type operates at full load with a gear speed of about 35 r/min and a load of about 27 KN. In the numerical simulation, the direction of the rotational speed of section I is set to be X-axis forward, the direction of the load force is set to be Y-axis forward, and the setting of section II is the opposite to that of section I. On the other hand, although gear lubrication can reduce friction and improve efficiency (Liu et al., 2020), the actual lubrication of the gear and rack is very poor due to cost considerations. Therefore, the numerical simulation does not consider the role of lubrication oil.

The impact process of the gear and rack is shown in Figures 5 and 6. To facilitate the analysis, the time of the two calculation sections is normalized, i.e., the time at the beginning of the impact is assumed to be $\tau = 0$. It can be seen that the meshing impacts all occur in the area between the index circle and the tooth root of the gear, as well as at the tooth top part of the rack,

which is consistent with the actual situation. However, the impact site of the rack in section II is a little further away from the top surface of the tooth, which will make the contact area of the gear and rack in section II larger than that in section I. Assuming that the magnitude of the impact force is the same for the two calculated sections, the impact stress in section I will be larger, which means that section I is more prone to structural damage. The next analysis precisely verifies this point.

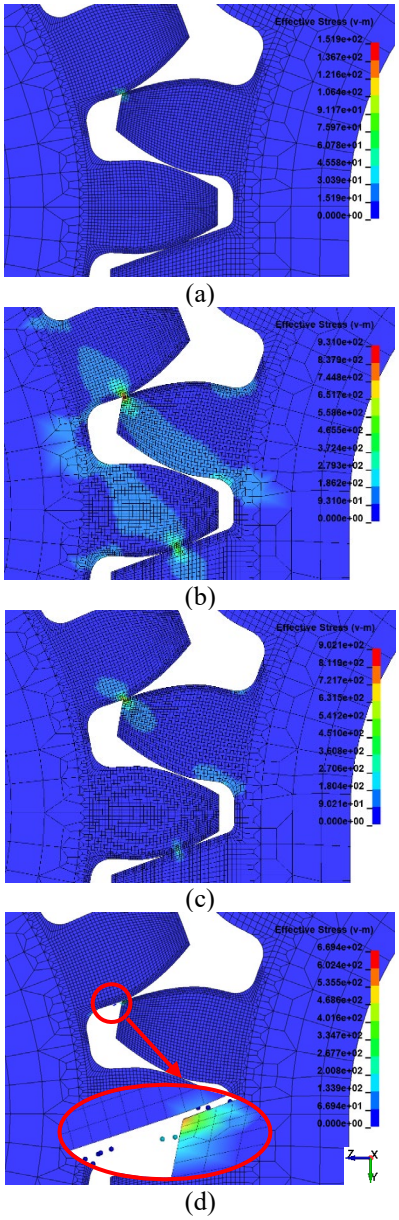

Fig. 5. Meshing impact process in section I: (a) τ=0, (b) τ=0.2ms, (c) τ=0.4ms, (d) τ=0.6ms.

After the start of the impact, stresses are generated at the contact point, as shown in Fig. 5(a) and 6(a). However, the stresses seem to be generated in other parts of the gear in the figure, which is due to the larger size of the gear, thus leading to a more pronounced effect of inertia at the distal end of the gear when it is started. However, the values are small and therefore do not affect the numerical simulation results.

At 0.2ms after the onset of the impact, Fig. 5(b) and 6(b) show that the stresses propagate rapidly along the direction from the contact point of the contacting tooth pair to the root of the non-working surface, which is, in fact, the direction of the meshing line. Subsequently, due to the tensile effect, the stress propagates to the tooth roots on the working surface as well. Among them, the stress propagation in section II seems to be a little bit larger, which suggests that there is a stress concentration in section I. When the impact occurs at 0.4ms, the stress distribution area of section I is greatly reduced, and the stress at the root of the tooth begins to decrease, which indicates that section I is already in the stage of disengagement. For section II, from Fig. 6(c), the stress distribution area is only slightly reduced. This means that although section II is also in the disengagement stage of impact, it is disengaged more slowly, which means that the impact time of section II is longer than that of section I.

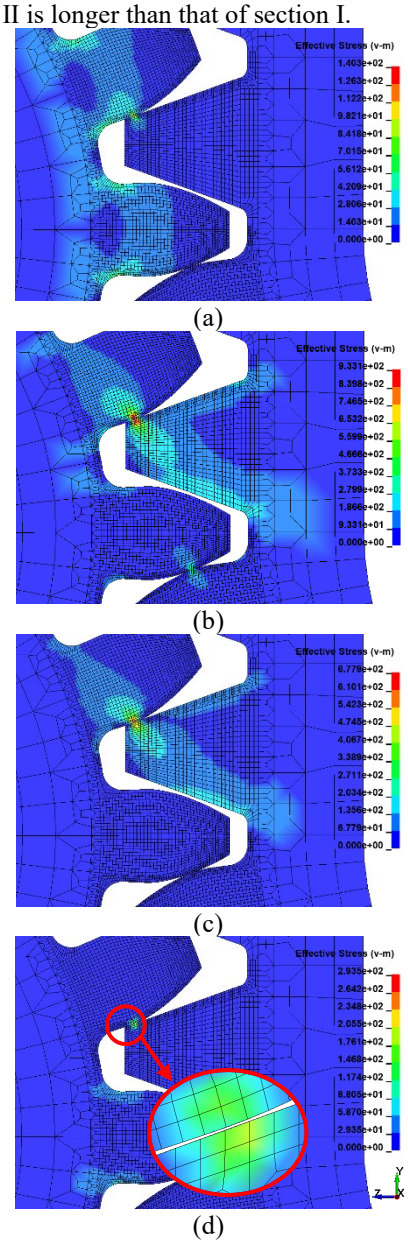

Fig. 6. Meshing impact process in section II: (a) τ=0,

(b) τ=0.2ms, (c) τ=0.4ms, (d) τ=0.6ms.

When the impact occurs after 0.6ms, the gear and rack in the two calculation sections are completely disengaged from contact, and most of the regional stress disappears with the disappearance of the force. However, in both Fig. 5(d) and Fig. 6(d), there is still stress near the contact part of the gear and rack. It indicates that residual stresses are present in both calculation sections, which is a bad sign for the structural integrity of the material. Residual stress has many hazards, including its impacts on the mechanical properties of materials and the dimensional accuracy of components. First, when there is tensile residual stress in a material, it will reduce its tensile yield strength while correspondingly increasing the compressive yield limit. Second, residual tensile stress will shift the stress cycle of variable loads, resulting in a decrease in fatigue strength. When there is residual tensile stress in a gear, its fatigue resistance will be significantly reduced. Third, the presence of residual stress increases the brittleness of the material, reducing its toughness and ductility. Fourth, during the service process, the relaxation of residual stress will cause changes in the dimensions and shapes of gears and racks, affecting their dimensional stability. Therefore, on the one hand, the presence of residual stresses will lead to greater stresses in the area when it is subjected to the next impact; on the other hand, the material in the area may have undergone plastic deformation and the material properties are degraded. The combination of these two factors makes the area more susceptible to structural damage, including material slippage and spalling.

In addition to this, it should be noted that the pairs of teeth shown to be meshing in Figs. 5(a) and 6(a) do not make contact, but do so at a subsequent time. This is not in accordance with the laws of gear meshing. The reason for this is analyzed to be that the rack here is not properly constructed. Since the rack is made up of a straight rack and an incomplete gear, it has not been treated in any way that would constitute a condition for the occurrence of a meshing impact.

Of course, Fig. 5(d) can be seen clearly: section I has SPH particles generated during the impact process and is involved in the calculation. Therefore, section I is the focus of the next analysis. When the impact was carried out to 0.42ms, a FEM cell at the top of the rack near the forward end of the X-axis was deleted and the first SPH particle was generated, as shown in Fig. 7(a). Subsequently, other parts evolve rapidly. By 0.44 ms, the seventh SPH particle is generated, as shown in Fig. 7(b). When the impact proceeds to 0.46ms, the twelfth SPH particle is generated, as shown in Fig. 7(c). All the physical information of the deleted FEM cell is inherited by the newly generated SPH particle, which executes the SPH algorithm and couples with other FEM cells until the end of the simulation.

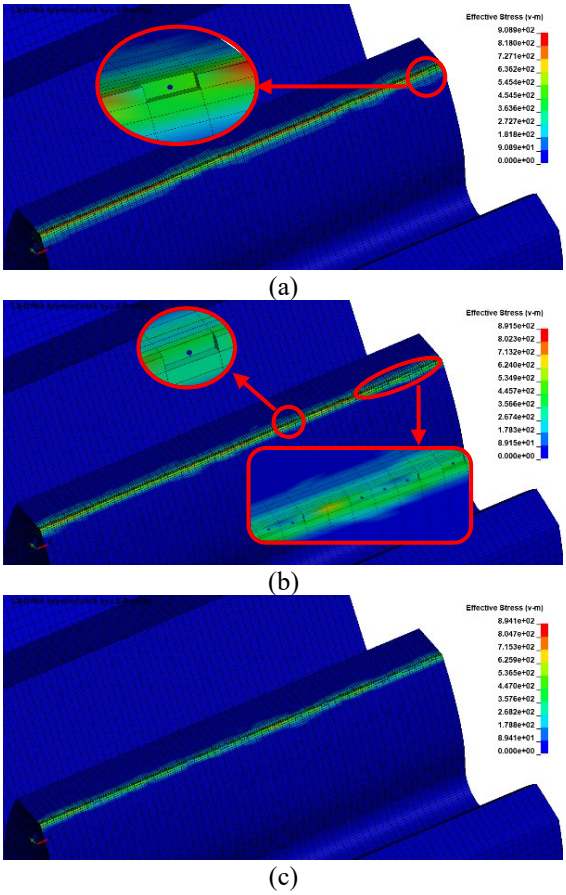

Fig. 7. SPH particle generation process: (a) τ=0.42ms, (b) τ=0.44ms, (c) τ=0.46ms.

From Fig. 7, it can be found that the failure of the FEM unit is not the failure of all units in the X direction on the contact surface together, but extends irregularly from one side of the rack end face to the other. Secondly, in conjunction with Fig. 9, it can be seen that no new SPH particles are produced in the gear and rack since the impact is up to 0.46 ms. Therefore, the amount of material failure is very small during the whole impact process, which is very consistent with the real situation. These newly generated SPH particles represent the material debris spalling from the localized region of the rack tooth top, and so on, and the amount of material spalling increases after several impacts, which is manifested as the wear of the tooth top from a macroscopic point of view. This reasoning is verified by Figure 8, which shows the wear of the rack in reality.

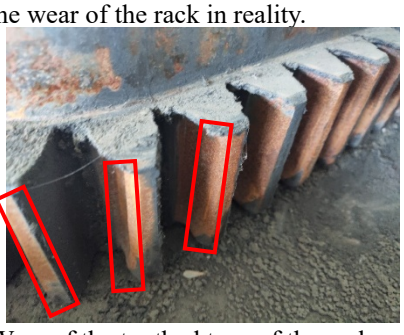

Fig. 8. Wear of the toothed tops of the rack.

Fig. 9 shows another angle of Figure 5(d). At this

point, two particular particles are found, which are circled by the red line box. They are considered special because there are residual stresses in them, while the other particles are already in a zero-stress state. The positional information of these two particles is extracted as shown in Fig. 10(a), and the two particles are labeled successively as α and β along the X-positive direction. It can be seen that α and β are generated at the same time. Their position changes in the X direction are almost symmetric, and the magnitude of the changes in the X direction is smaller compared with the other two directions. In the Y-direction, both α and β move generally in the positive direction. Among them, β moved 0.1 mm to the negative direction of the Y-axis when it was first generated, but changed its motion direction within a short time. α and β moved in the Z-direction in approximately the same way as in the Y-direction, but the motion process was more convoluted, especially for α. To analyze the motion process of α and β more intuitively, Fig. 10(b) shows their trajectories in the ZY-plane, and the reason why the X-direction was not taken into account is that the particles in the X-direction will not collide with other objects in the X direction. For Fig. 10(b), those places where there is an abrupt change in the direction of particle motion need extra attention. Among them, α has a more zigzag trajectory and has a lower probability of colliding with the rack, while β collides with both the gear and the rack. Figure 11 shows the time evolution of the velocities of α and β. The velocity profiles show that β collides at the very beginning, and in conjunction with Figure 10 it can be seen that the collision is with the gear; likewise for α, but with a little less collision force. In summary, the debris generated by the gear and rack after impact will have multiple collisions with nearby structures.

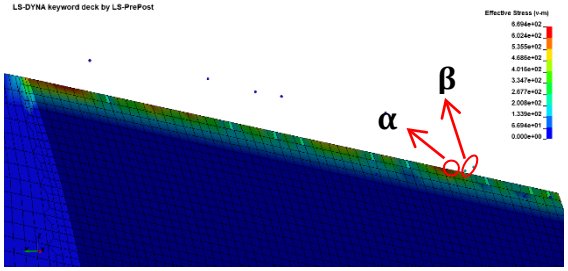

Fig. 9. Another view of section I at τ = 0.6 ms.

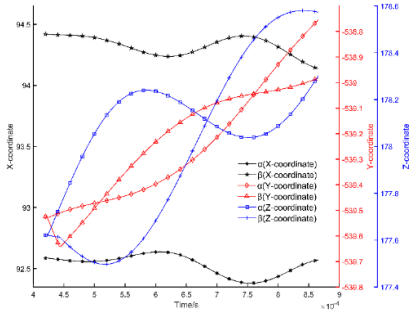

(a)

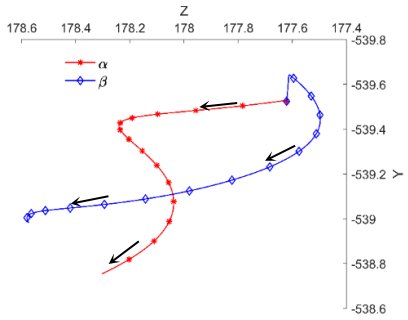

(b)

Fig. 10. Positional information of α and β: (a) 3D coordinate changes of α and β; (b) trajectories of α and β in the ZY plane.

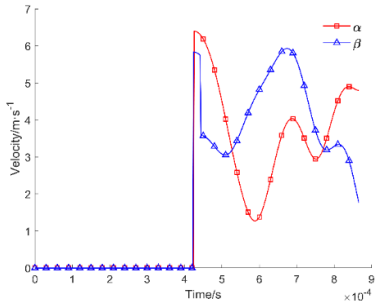

Fig. 11. Velocity variation of α and β.

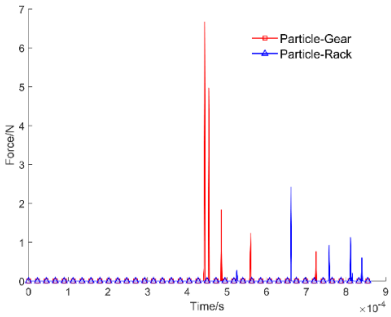

Fig. 12. Impact of SPH particles on gear and rack.

There is another piece of information in Fig. 11 that should not be ignored: the velocity of the particles is not high, and the impact of the collisions generated by the particles with the gear and rack at low velocities may be small. To verify this inference, the combined impact of the particles on the gear and rack is extracted, as shown in Fig. 12. It can be found that when the particles are first generated, the collisions mainly occur between the particles and the gears; as time passes, the collisions start to occur between the particles and the racks. The impact ensemble force between the particle and the gear is overall larger than that of the rack, however, the impact ensemble force is much smaller than the impact meshing force between the gear and the rack regardless of whether it is relative to the gear or the rack, and both decrease with time, indicating that the particles gradually disengage from the meshing region of the gear and the rack. In conjunction with Figure 10, it can be seen that the debris represented by these particles will eventually fall on other gear surfaces, and in reality, there will be lubricating oil on the surface of the gear and rack, so

this debris will be easily absorbed by the lubricating oil and will fuse with multiple debris or windborne sand particles to form a mixture block during the gear movement. These clumps in turn can grow in size over time and may cause damage to the tooth surfaces as the gear and rack mesh, especially if a meshing impact occurs. According to surveys, this is a real-life occurrence.

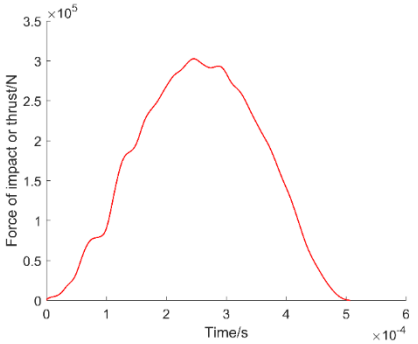

(a)

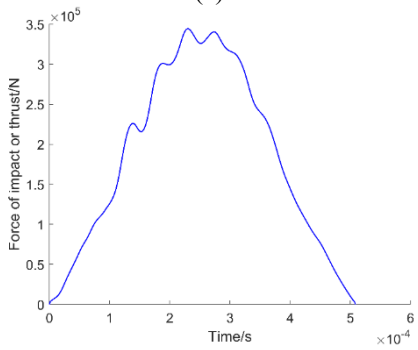

(b)

Fig. 13. Meshing impacts of gear and rack: (a) section I, (b) section II.

The impact force is an important parameter in the impact behavior, therefore, Fig. 13 demonstrates the impact force in section I and section II. It can be seen that the trend of the impact force obtained by the adaptive SPH-FEM coupling algorithm is in good agreement with the literature (Tang et al., 2007). In particular, the impact force of section II is higher than that of section I, and the oscillation amplitude of the impact force of section II is also more intense. This indicates that although the structure of section II is a little bit more robust, the gears experience severe vibration when meshing up to this point.

MICROSCOPIC MODEL EXPERIMENT

According to Table 2, it can be seen that the gear and rack have huge dimensions and the load forces applied are too large to perform 1:1 experiments, so in this paper, the miniaturization experiments (Wen et al., 2019) are used to verify the rationality of the adaptive SPH-FEM coupling method. The miniaturization method involves shrinking the gear and rack along the three translational degrees of freedom in three-dimensional space in the ratio of 8:1, so the load force applied for the experiment is about 53N (Ke et al., 2010). Since the angular velocities were applied to the rotational degrees of freedom, the experimentally applied angular velocities were the same as in the numerical simulations. It is worth noting that the number of teeth of the rack is so large that it is still difficult to produce even after reduction, and since this paper only deals with the meshing impacts in the transition section, only the part of the rack close to the transition section is used for the experiments, as shown in Fig. 14. The meshing impact force between the gear and rack measured in the experiment is shown in Fig. 16, in which the experimental data are normalized. Table 4 shows the peak impact force for both methods.

Fig. 14. Gear and rack used for the experiment

Fig. 15. Impact force data acquisition system.

It can be seen that the peak impact force obtained by the two methods is not much different from each other, the error is within the acceptable range, and the shape of the impact force curve is roughly the shape of a single pulse sinusoidal curve. However, the impact time of the experiment is generally longer, the arrival time of the peak impact force is more lagging, and the impact force oscillates more violently, which may be due to the experimental device in the assembly of a certain error. Overall, both the numerical magnitude and the overall trend of the impact force, the numerical simulation results and the experimental results are roughly the same, indicating that the numerical simulation in this paper has a high degree of reliability.

Table 4. Comparison of peak impact forces. (unit: ×83 N)

	Simulated values	Experimental values	Experimental values
Section I	591.31	552.98	6.48
Section II	672.50	637.33	5.23

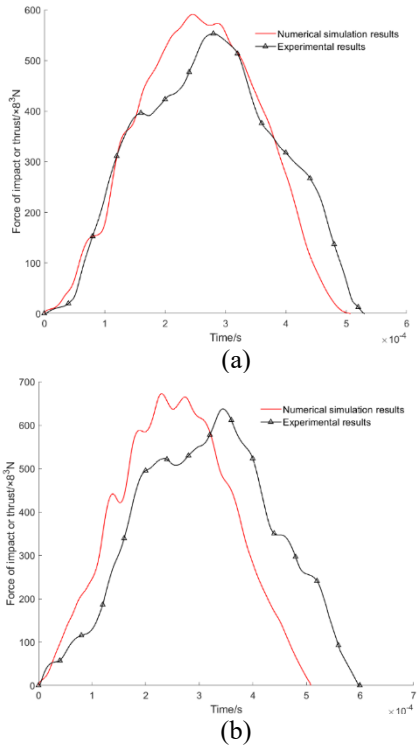

Fig. 16. Comparison of impact force: (a) Section I, (b) Section II.

CONCLUSIONS

In this paper, the pumping machine rack and pinion meshing impact is simulated by an adaptive SPH-FEM coupling method, and micro-experiments are designed to verify the effectiveness of the method. The study shows:

(1) Transition section damage mechanism: from straight line to circular arc transition section (I) is more prone to local material spalling, the peak residual stress is 6.694×10^2 MPa, and from circular arc to straight line section (II) there is no structural damage but the vibration is more significant;

(2) Influence of metal debris: The impact of spalling debris is limited by the low velocity of a single impact, but the mixed mass formed by its accumulation will be embedded in the tooth surface, inducing pitting and other defects;

(3) Advantage of the method: Compared with the traditional FEM, the coupled adaptive SPH-FEM method can accurately track the physical information of the spalled material, and the error of the peak impact force is less than 5%.

The current material failure criterion is based on critical plastic strain, and a more systematic metal failure model is needed to improve the simulation accuracy in the future. This method provides a new idea for the impact study of gears with structural damage, and can be further optimised with engineering feedback.

REFERENCES

Bai, Y. S., Ahmat, M., Bai, H. Y., et al., "Stress and fatigue life analysis of pitting defects in pumping gears," *Mechanical Strength*, vol. 44, no. 3, pp. 713–718, (2022).

Feng, R. F., Fourtakas, G., Rogers, B. D., et al., "Two-phase fully coupled smoothed particle hydrodynamics (SPH) model for unsaturated soils and its application to rainfall-induced slope collapse," *Computers and Geotechnics*, vol. 151, p. 104964, (2022).

Guo, Q., "Handbook of Chinese and Foreign Metallic Materials," 1st ed., Chemical Industry Press: Beijing, (2015).

Hu, S. Y., Fang, Z. D., Xu, Y. Q., et al., "Meshing impact analysis of planetary transmission system considering the influence of multiple errors and its effect on the load sharing and dynamic load factor characteristics of the system," *Proceedings of the Institution of Mechanical Engineers, Part K: Journal of Multi-Body Dynamics*, vol. 235, no. 1, pp. 57–74, (2021).

Han, D., Rong, S. F., Rong, K. B., et al., "Sensitive misalignment-based dynamic loaded meshing impact diagnosis mechanism for aviation spiral bevel gear transmission," *Expert Systems with Applications*, vol. 200, p. 116969, (2022).

Jia, C., Yao, L. Z., Zhang, J., et al., "Modified involute helical gear meshing impact calculation," *Journal of Xi'an Jiaotong University*, vol. 54, no. 09, pp. 58–65+80, (2020).

Kim, S. I., Lee, Y., and Byon, S. M., "Study on constitutive relation of AISI 4140 steel subject to large strain at elevated temperatures," *Journal of Materials Processing Technology*, vol. 140, no. 1–3, pp. 84–89, (2003).

Ke, H. C., Yang, Y. M., Ke, G., et al., "Application of miniature scale experimental model in air-conditioning engineering," *Proceedings of the 30th Anniversary of the Establishment of the Beijing Institute of Refrigeration and the 10th Annual Academic Conference, Beijing Institute of Refrigeration*, pp. 141–144, (2010).

Liu, X., Fang, Z. D., Yin, X. M., et al., "A novel calculation method of long-period pinion axial displacement and meshing impact force for double-helical gear considering asymmetry error," *Mechanism and Machine Theory*, vol. 171, p. 104775, (2022).

Lu, Y. S., Zhu, Z. W., and Xie, Q. J., "Study on the dynamic constitutive relationship of 42CrMo steel based on improved J-C model," *Journal of Sichuan Institute of Technology (Natural Science Edition)*, vol. 29, no. 3, pp. 61–65, (2016).

Liu, H. L., Liu, H. J., Zhu, C. C., et al., "Effects of lubrication on gear performance: A review,"

Mechanism and Machine Theory, vol. 145, p. 103701, (2020).

Mustafa, B., Ozturk, F., Demirezen, M., et al., "Analysis of tempering treatment on material properties of DIN 41Cr4 and DIN 42CrMo4 steels," *Journal of Materials Engineering and Performance*, vol. 16, no. 5, pp. 597–600, (2007).

Peng, Y. and Wang, L., "A gear and rack pumping unit design," *Advanced Materials Research*, vol. 472–475, pp. 657–661, (2012).

Qiang, H. F., "New Methods and Applications of Smoothed Particle Hydrodynamics," 1st ed., Science Press: Beijing, (2017).

Rahimi, M. N. and Moutsanidis, G., "Modeling dynamic brittle fracture in functionally graded materials using hyperbolic phase field and smoothed particle hydrodynamics," *Computer Methods in Applied Mechanics and Engineering*, vol. 401, p. 115642, (2022).

Ren, G. F., Wang, Y. X., Tang, Y. Q., et al., "Research on lateral bearing behavior of spliced helical piles with the SPH method," *Applied Sciences*, vol. 12, no. 16, p. 8215, (2022).

Tang, J. Y., Liu, X., and Dai, J., "An ANSYS/LS-DYNA-based impact study of gear drives with out-of-line meshing," *Vibration and Shock*, vol. 9, pp. 40–44+50+169, (2007).

Tang, Y. F., Hu, G. Z., Cao, X. Q., et al., "A study of SPH numerical algorithm for dynamic meshing and transmission analysis of rack and pinion," *Vibration and Shock*, vol. 40, no. 16, pp. 39–44, (2021).

Wang, C. D., He, Z. Y., Yang, Z., et al., "Calculation method for impact excitation of loaded gear pair," *Journal of Aerospace Dynamics*, pp. 1–10, (2023).

Wałęsa, K., Górecki, J., Berdychowski, M., et al., "Modelling of the process of extrusion of dry ice through a single-hole die using the Smoothed Particle Hydrodynamics (SPH) method," *Materials*, vol. 15, no. 22, p. 8242, (2022).

Wen, W., Jackson, G. A., Li, H., and Sun, W., "An experimental and numerical study of a CoNiCrAlY coating using miniature specimen testing techniques," *International Journal of Mechanical Sciences*, vol. 157–158, pp. 348–356, (2019).

Xiao, N., Zhou, X. P., and Gong, Q. M., "The modelling of rock breakage process by TBM rolling cutters using 3DFEM-SPH coupled method," *Tunnelling and Underground Space Technology*, vol. 61, pp. 90–103, (2017).

Xin, C. L., "Handbook of Common Material Parameters for Finite Element Analysis," 1st ed., Mechanical Industry Press: Beijing, (2020).

Zhou, C., Tang, J., Yuan, J., and Zhong, C., "Extra-linear meshing and impact friction in gearing," *Journal of Mechanical Engineering*, vol. 3, pp. 75–81, (2008).

Zhou, Y. D., Sun, Y. C., Huang, T. L., et al., "SPH-FEM simulation of impacted composite laminates with different layups," *Aerospace Science and Technology*, vol. 95, p. 105469, (2019).

Zhang, Z. C., Qiang, H. F., Fu, X. J., et al., "Numerical computation of the impact of a 7.62 mm rifle bullet on a 30CrMnSiA steel plate based on the SPH-FEM transformation algorithm," *Computational Physics*, vol. 29, no. 1, pp. 73–81, (2012).